

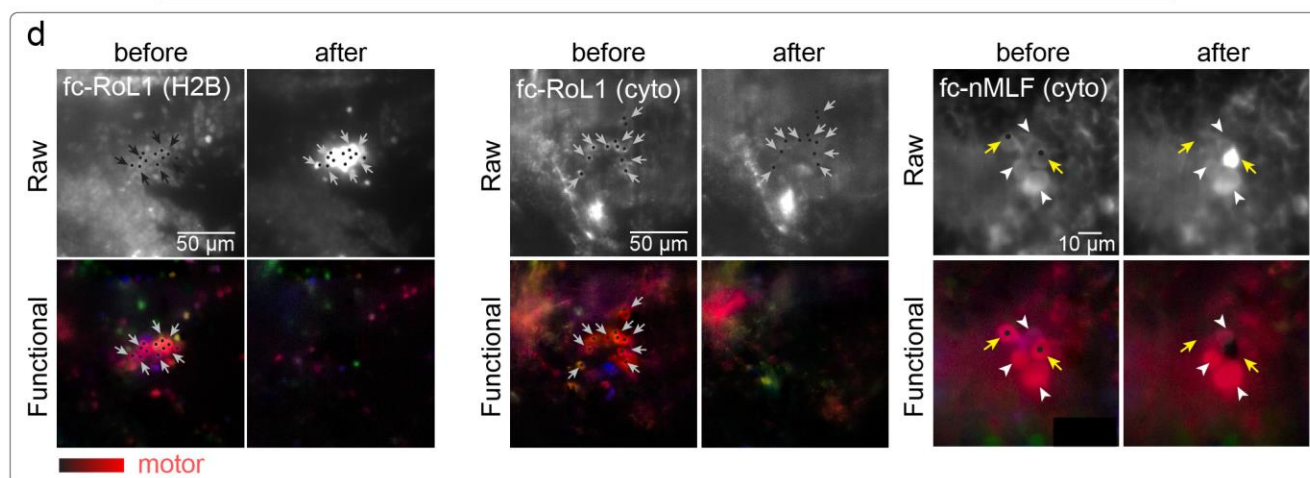
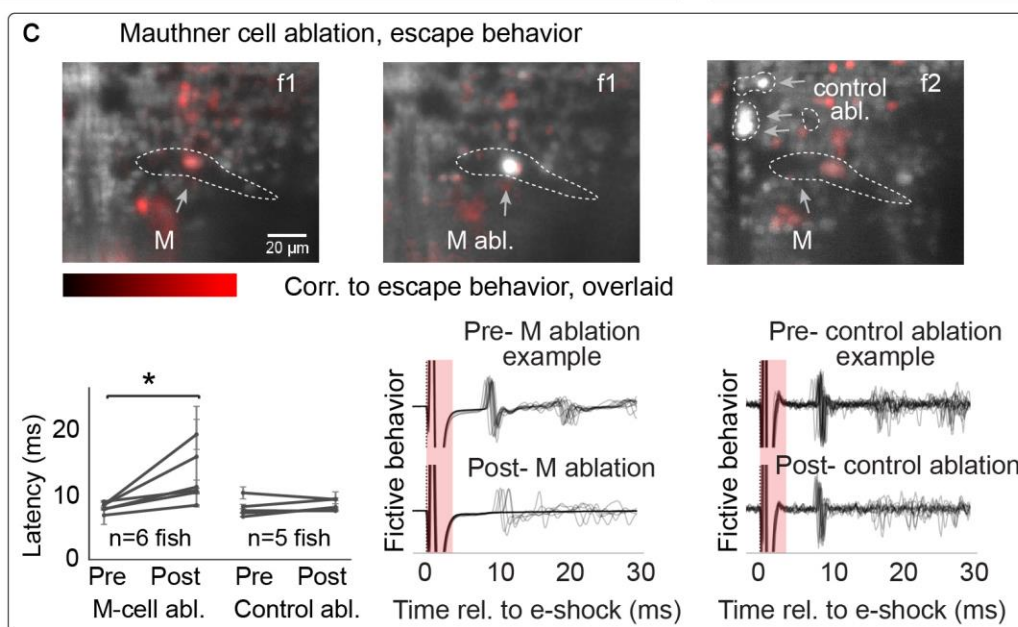
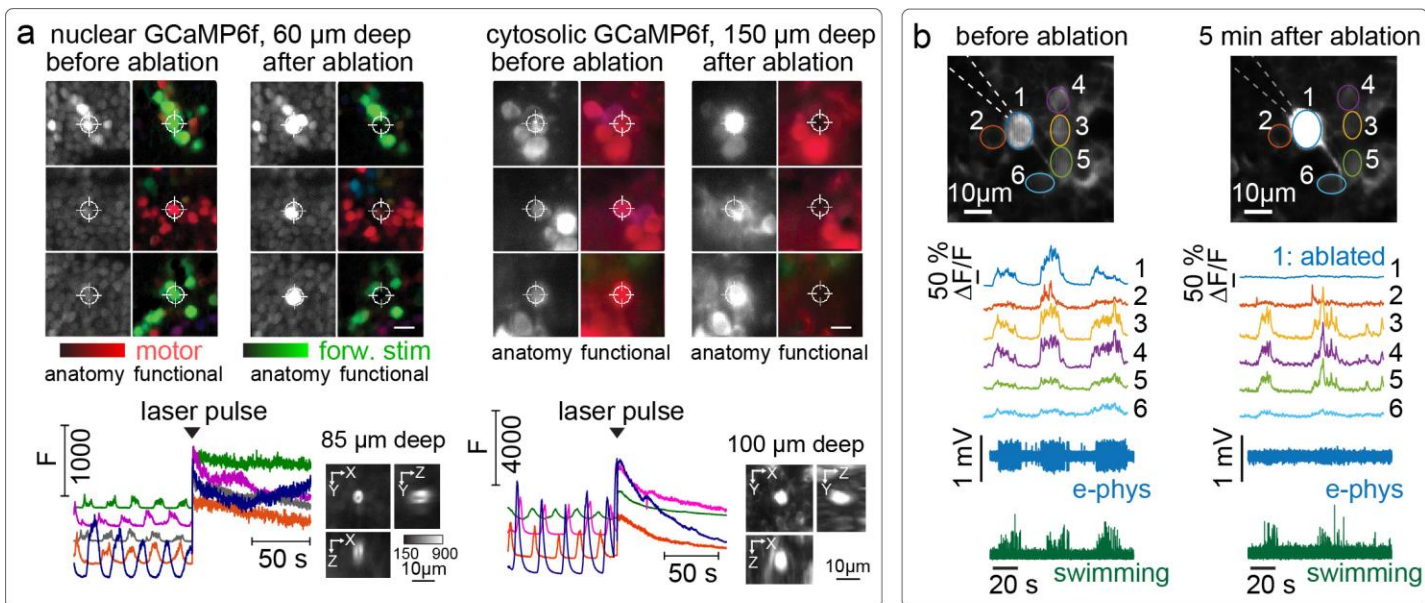
In the format provided by the authors and unedited.

# Brain-wide circuit interrogation at the cellular level guided by online analysis of neuronal function

Nikita Vladimirov <sup>1,4,6\*</sup>, Chen Wang<sup>1,6</sup>, Burkhard Höckendorf<sup>1,6</sup>, Avinash Pujala<sup>1</sup>, Masashi Tanimoto<sup>1,2</sup>, Yu Mu <sup>1</sup>, Chao-Tsung Yang<sup>1</sup>, Jason D. Wittenbach<sup>1</sup>, Jeremy Freeman<sup>1,5</sup>, Stephan Preibisch <sup>3</sup>, Minoru Koyama<sup>1</sup>, Philipp J. Keller <sup>1,7\*</sup> and Misha B. Ahrens <sup>1,7\*</sup>

---

<sup>1</sup>Janelia Research Campus, Howard Hughes Medical Institute, Ashburn, VA, USA. <sup>2</sup>Nagoya University, Nagoya, Japan. <sup>3</sup>Berlin Institute for Medical Systems Biology (BIMSB), Max Delbrück Center for Molecular Medicine in the Helmholtz Association (MDC), Berlin, Germany. <sup>4</sup>Present address: Berlin Institute for Medical Systems Biology (BIMSB), Max Delbrück Center for Molecular Medicine in the Helmholtz Association (MDC), Berlin, Germany. <sup>5</sup>Present address: Chan Zuckerberg Initiative, San Francisco, CA, USA. <sup>6</sup>These authors contributed equally: Nikita Vladimirov, Chen Wang, Burkhard Höckendorf. <sup>7</sup>These authors jointly supervised this work: Philipp J. Keller, Misha B. Ahrens. \*e-mail: [nikita.vladimirov@gmail.com](mailto:nikita.vladimirov@gmail.com); [kellerp@janelia.hhmi.org](mailto:kellerp@janelia.hhmi.org); [ahrensm@janelia.hhmi.org](mailto:ahrensm@janelia.hhmi.org)



## Supplementary Figure 1

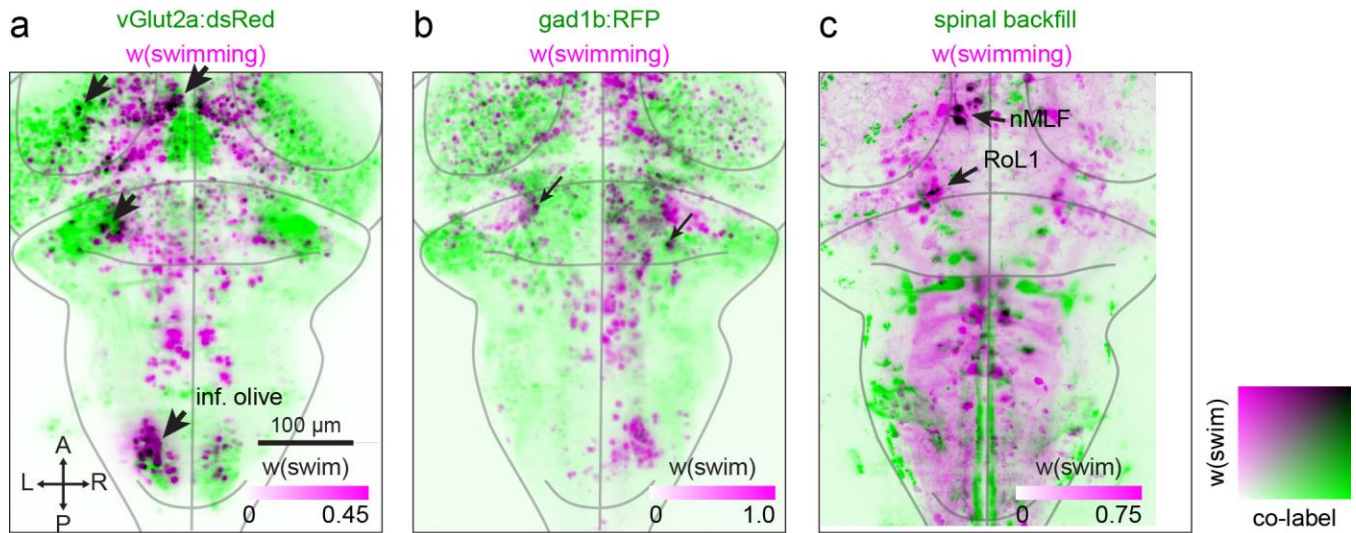
Single-cell-ablation accuracy for population ablations

**a**, Single-cell accuracy of two-photon laser ablation. Similar data as in **Fig. 1d**, but additionally showing cytosolic examples. The increase in fluorescence in cytosolic-expressing cells lasts for a shorter period than in nuclear-expressing cells. Scale bars, 10  $\mu\text{m}$ .

**b**, Electrophysiological verification of single-cell resolution of two-photon ablation. Same data as in **Fig. 1f**, this time including fluorescence traces from nearby cells.

**c**, Mauthner cell ablation and control experiments (top row). The Mauthner cell was functionally identified within the reticulospinal region in *Tg(elav13:H2B-GCaMP6f)* *relaxed* mutants (shown in red). Ablated cells are visible by their increase in brightness. (bottom row) Behavioral latency increases significantly after Mauthner cell ablation, but not after control cell ablation (means and 95% confidence intervals are shown; Mauthner ablation:  $p=0.027$ ; control:  $p=0.345$ ; Wilcoxon signed-rank test, asterisk indicates  $p<0.05$ ). Examples of fictive behavior traces after Mauthner cell ablation and control ablations are shown.

**d**, Single-cell resolution of ablation is preserved when ablating multiple nearby cells, both in nuclear-localized expression of the calcium indicator (left) and cytosolic expression (middle, right). Dots show the ablation coordinates, arrows are added for clarity. For both ablation types, cell brightness initially increases and eventually decreases; in the case of cytosolic expression, brightness decreases faster, visible in the example (middle and right).



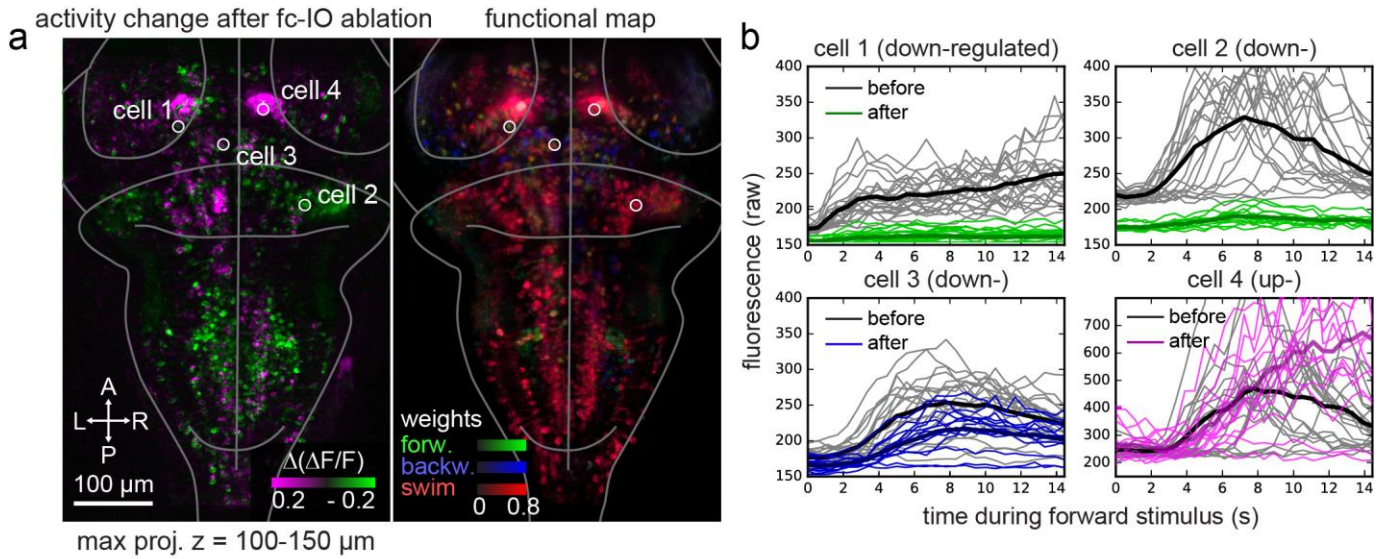
### Supplementary Figure 2

Two-color imaging of double-transgenic fish expressing neurotransmitter markers in red (glutamatergic *vGlut2a* or GABAergic *gad1b*) or spinal backfill, overlaid with a functional map for swimming computed from GCaMP6f imaging

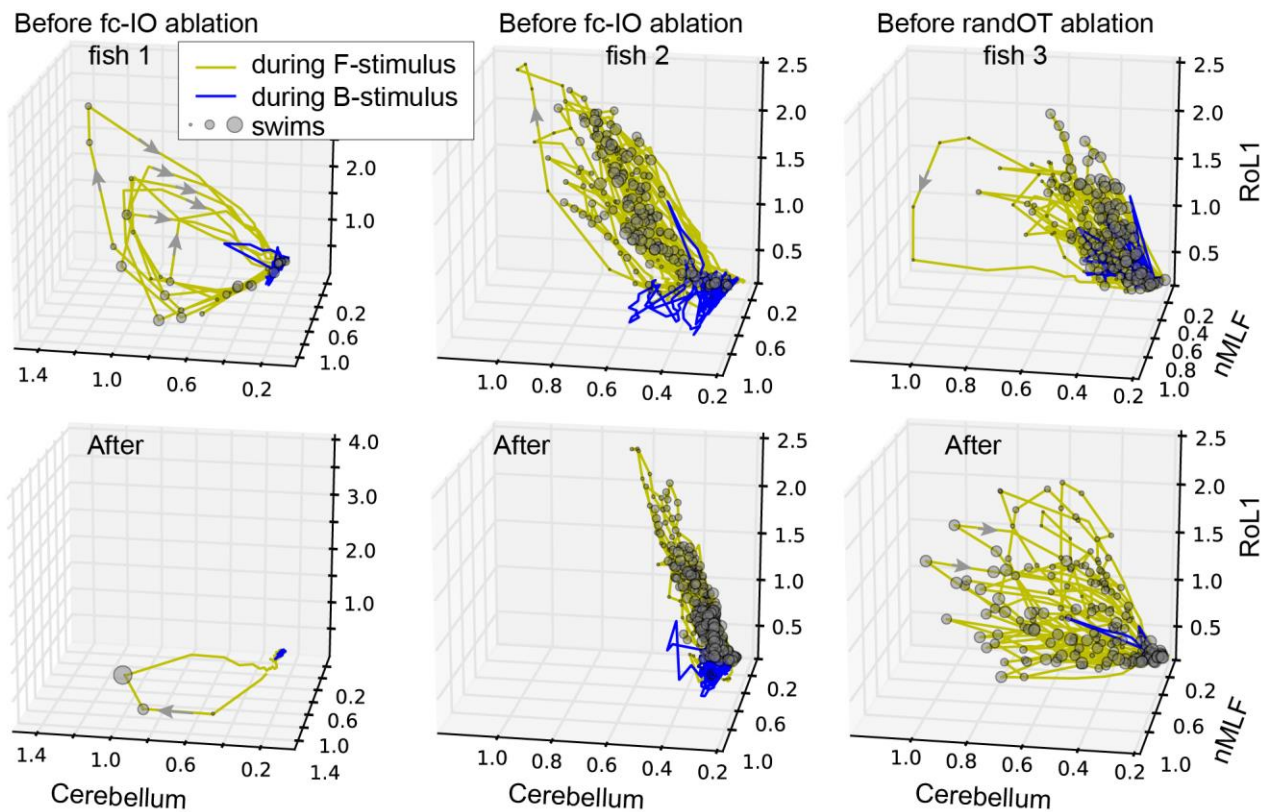
**a**, Overlay of neurons active during swimming and a glutamatergic marker (colocalization is black, e.g. arrows).

**b**, Overlay of neurons active during swimming and a GABAergic marker (colocalization at e.g. arrows).

**c**, Spinal cord backfill with Texas Red dye shows that fc-RoL1 (tuned to swimming) includes RoL1 cells, and fc-nMLF includes cells of the nMLF reticulospinal group.



**C**  $\Delta F/F$  trajectories in selected brain areas of example fish



**Supplementary Figure 3**

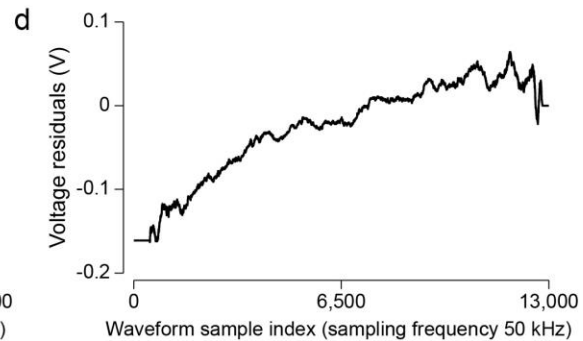
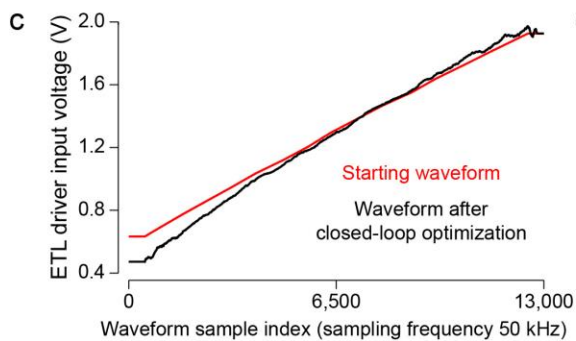
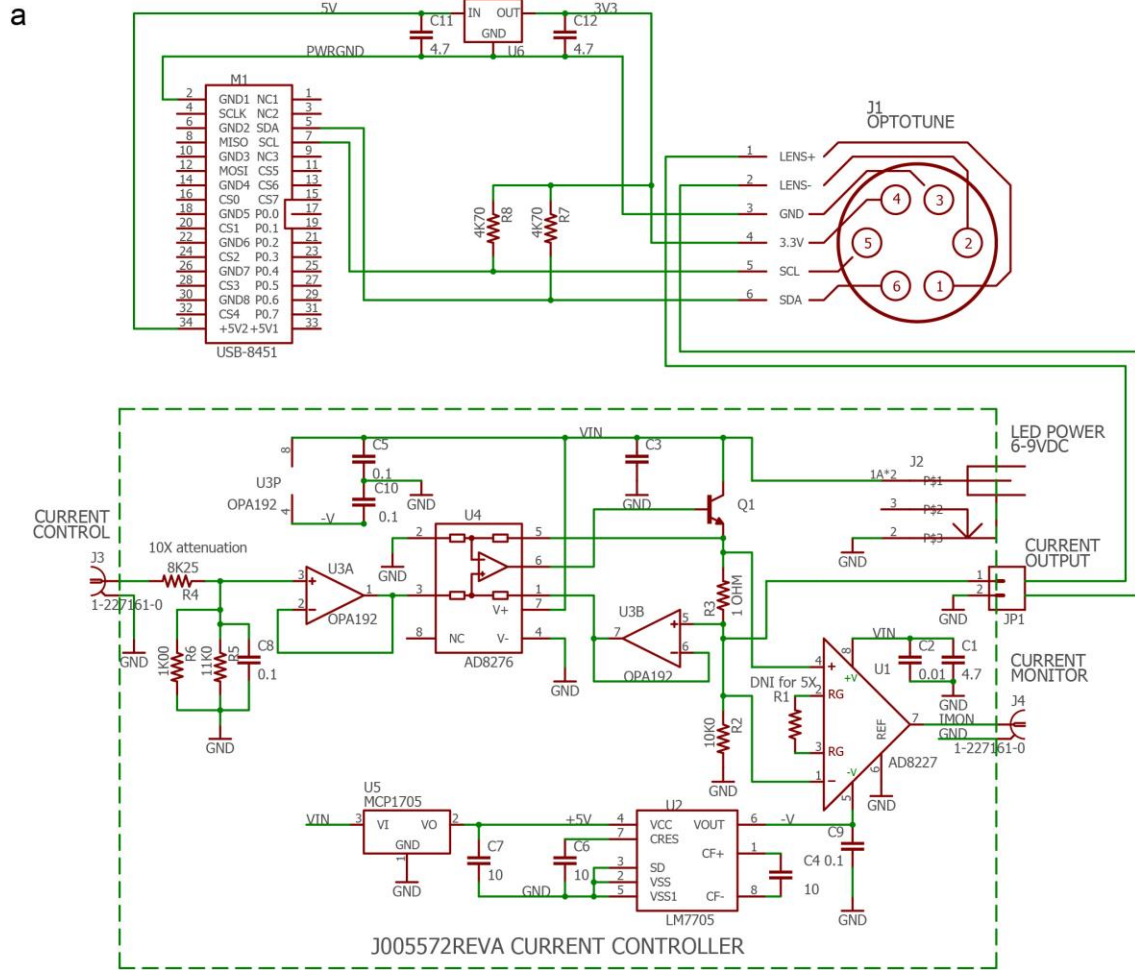
Changes in activity of individual neurons after ablation of motor-tuned cells in fc-IO

Neurons in the optic tectum (cell 1), cerebellum (cell 2), midbrain (cells 3 and 4) significantly change their response to forward-moving stimulus after fc-IO ablation.

**a**, Left: relative change in  $\Delta F/F$  (during the forward stimulus) before versus after ablation. Right: functional map.

**b**, Individual traces of neuron fluorescence and their averages over multiple trials (thick lines).

**c**, Examples of dynamics of  $\Delta F/F$  (top 95<sup>th</sup>-percentile of voxels in the region of interest over time) in the cerebellum, nMLF and RoL1 before and after inferior olive ablation (fish1, fish2) and random control ablations in the optic tectum (fish 3), arrows and the sizes of the circles indicate the flow of time. Experiments were done in *Tg(elavl3:GCaMP6f)* fish.



## Supplementary Figure 4

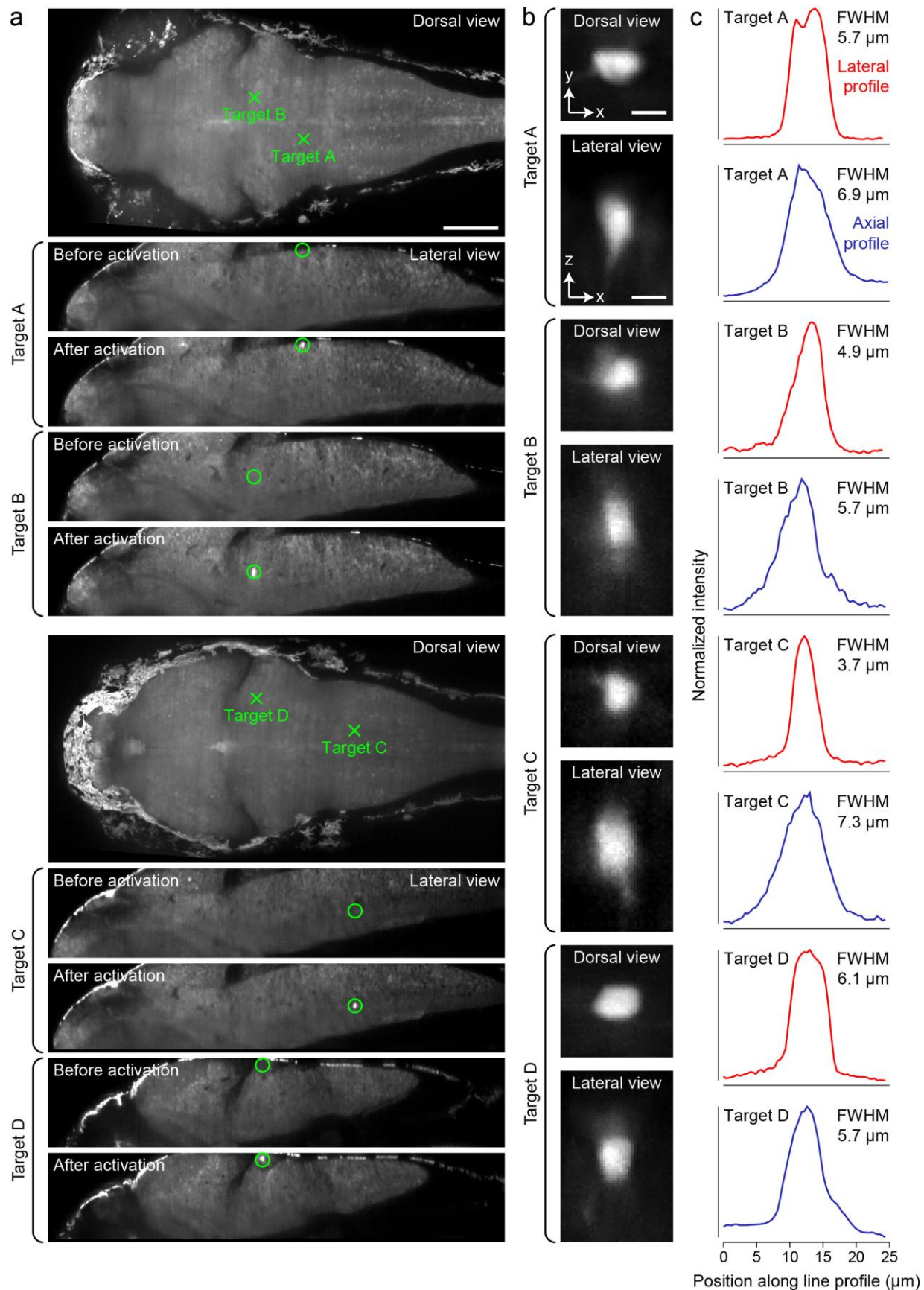
Custom ETL driver and closed-loop optimization of ETL waveforms

**a**, Schematic of the custom driver for high-speed, high-precision control of the electrical tunable lens (ETL).

**b**, Photos of the custom ETL driver.

**c**, Plots of the voltage waveform used to operate the ETL, before (red) and after (black) closed-loop optimization (representing the control voltage time course during one full volume acquisition). The starting waveform was determined with the calibration procedure described in methods section “Calibration procedure of the ETL-based 3D manipulation arm” and used as a starting point for closed-loop optimization. Waveform optimization during high-speed volumetric imaging was performed as described in methods section “Closed-loop optimization of ETL control waveform”. Input voltage to the ETL driver is controlled at a sampling rate of 50 kHz, i.e. the time interval between sample steps in the plot is 20  $\mu$ s. One volume scan takes 240 ms (corresponding to 12,000 samples; note that the waveforms shown here include 500 samples each preceding and succeeding the core volume scan). The focus stability obtained with this procedure during volumetric imaging is shown in **Fig. 5b**.

**d**, Time-dependent correction of voltage values determined by closed-loop optimization relative to the starting waveform (i.e. difference between black and red curves in panel c).



## Supplementary Figure 5

Characterization of the spatial extent of photostimulation during high-speed piezo-based volumetric imaging of photoactivatable-GFP-expressing larval zebrafish

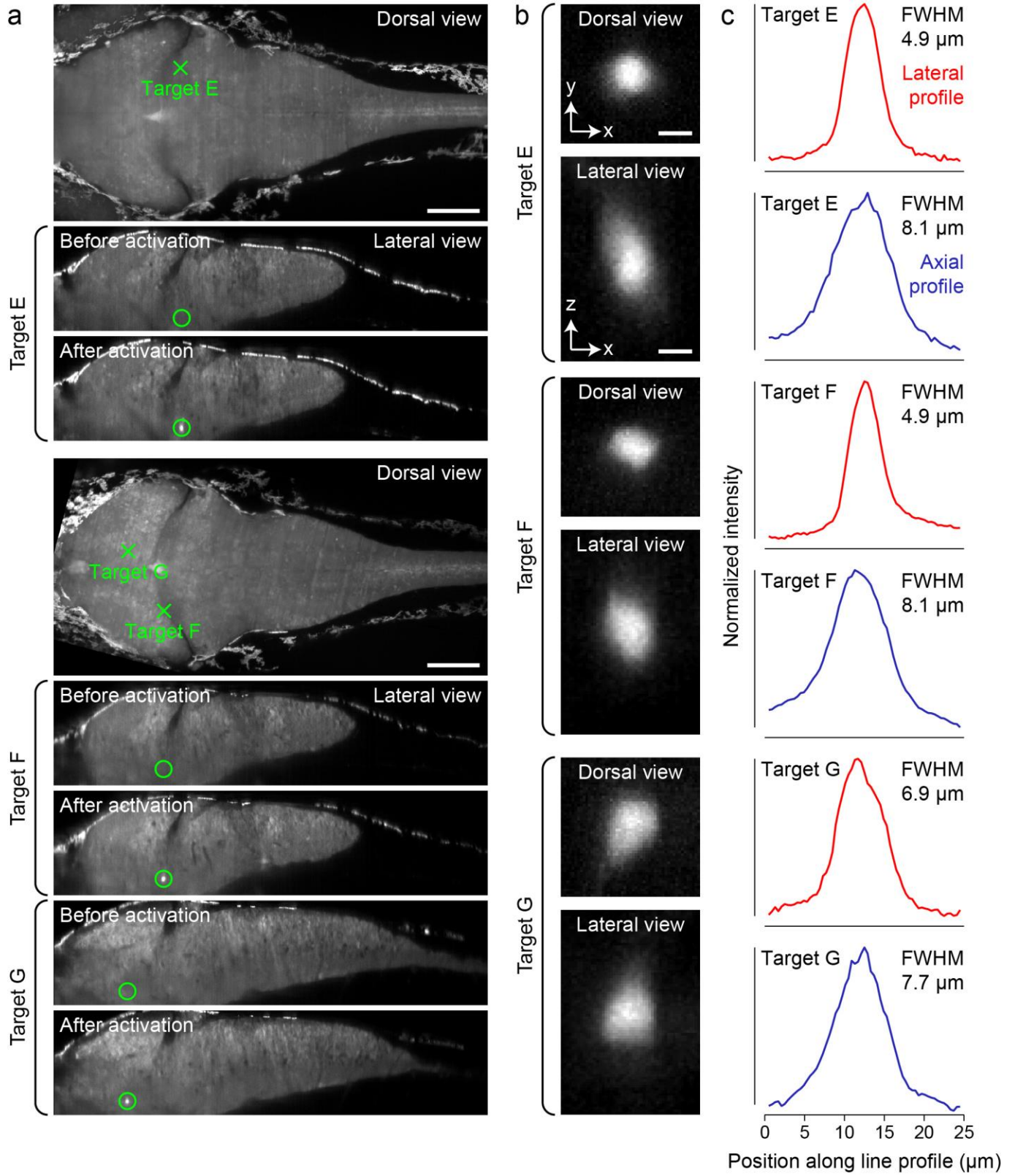
**a**, Dorsal-view maximum intensity projections and lateral-view slices of anatomy reference stacks acquired before and after photostimulation of targets in the brains of PA-GFP-expressing larval zebrafish. Targets A and B were photoactivated in the first specimen, and targets C and D were photoactivated in a second specimen. The depths of targets A, B, C, D relative to the surface of the brain were 20.5  $\mu\text{m}$ , 99.5  $\mu\text{m}$ , 101.5  $\mu\text{m}$  and 19  $\mu\text{m}$ , respectively.

**b**, Dorsal- and lateral-view maximum intensity projections of the photoactivated regions A, B, C and D.

**c**, Intensity profiles of photoactivated regions along lateral and axial directions and corresponding FWHM size. Overall, the spatial extent of activated regions (6-7  $\mu\text{m}$  axially and 4-6  $\mu\text{m}$  laterally) was found to be uniform across the brain and consistent with the resolution characterization based on a fluorescent dye shown in **Fig. 5**. The slightly smaller axial size of activated regions compared to the fluorescein-based resolution benchmark could arise from additional non-linear effects (with respect to laser power density) involved in the photoactivation of PA-GFP. The larger lateral size is the result of GFP diffusion in the cell's cytoplasm following photoactivation.

The experiment shown in this figure was repeated independently three times with similar results (for similar depths in the fish brain).

Scale bars, 100  $\mu\text{m}$  (a), 5  $\mu\text{m}$  (b).



**Supplementary Figure 6**

Characterization of the spatial extent of photostimulation deep inside the larval zebrafish brain

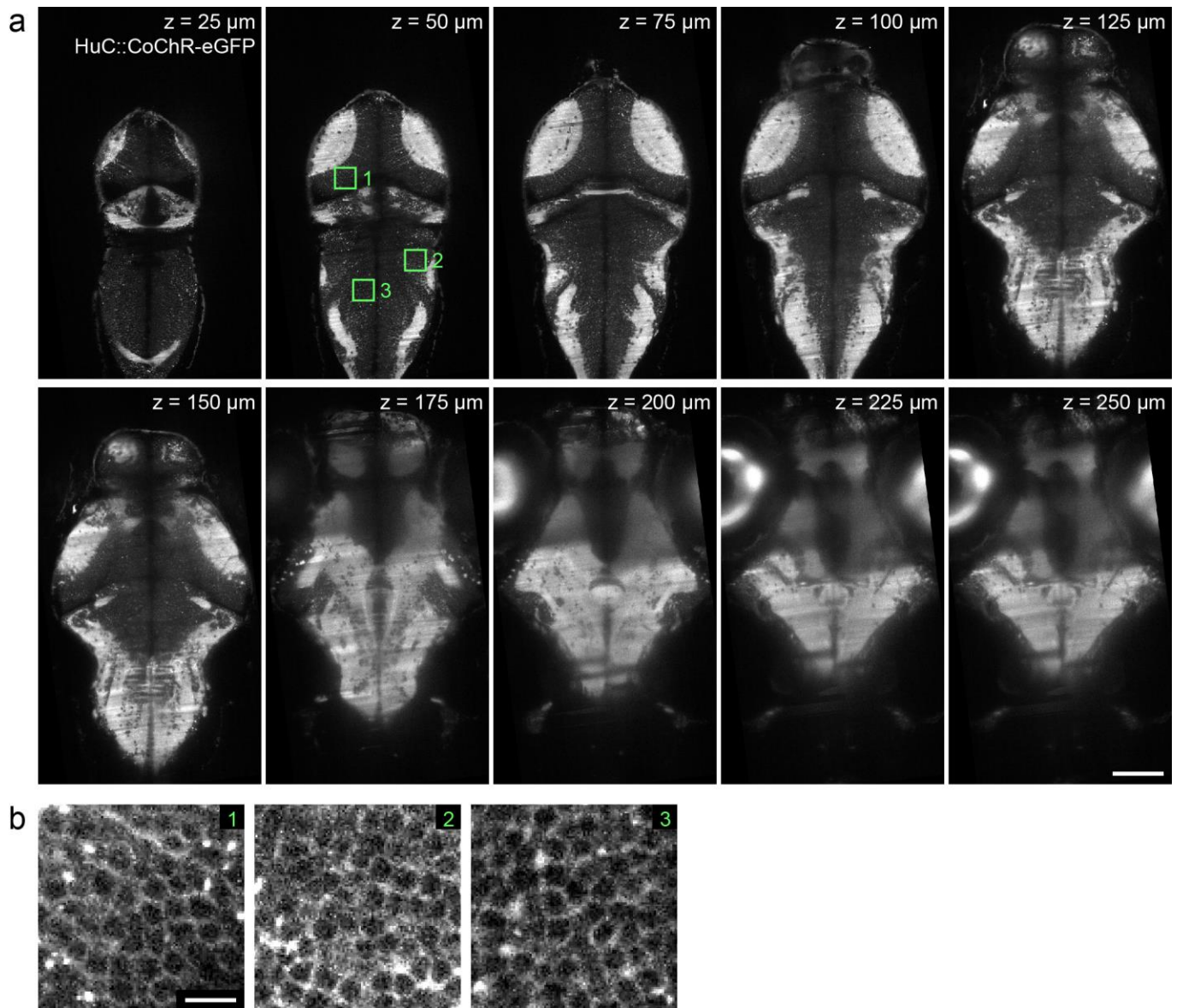
**a**, Dorsal-view maximum intensity projections and lateral-view slices of anatomy reference stacks acquired before and after photostimulation of targets in the brains of PA-GFP-expressing larval zebrafish. Target E was photoactivated in specimen #3, and targets F and G were photoactivated in specimen #4 (please see **SI Fig. 5** for targets A-D in specimens #1 and #2). The depths of targets E, F and G relative to the surface of the brain were 180.0  $\mu\text{m}$ , 172.5  $\mu\text{m}$  and 178.0  $\mu\text{m}$ , respectively.

**b**, Dorsal- and lateral-view maximum intensity projections of the photoactivated regions E, F and G.

**c**, Intensity profiles of photoactivated regions along lateral and axial directions and corresponding FWHM size. The spatial extent of activated regions (7-8  $\mu\text{m}$  axially and 5-7  $\mu\text{m}$  laterally) was found to be uniform across the brain and consistent with the resolution characterization based on a fluorescent dye shown in **Fig. 5** (please also see the legend of **SI Fig. 5c** in this context).

The experiment shown in this figure was repeated independently once with similar results (for similar depths in the fish brain).

Scale bars, 100  $\mu\text{m}$  (**a**), 5  $\mu\text{m}$  (**b**).



**Supplementary Figure 7**

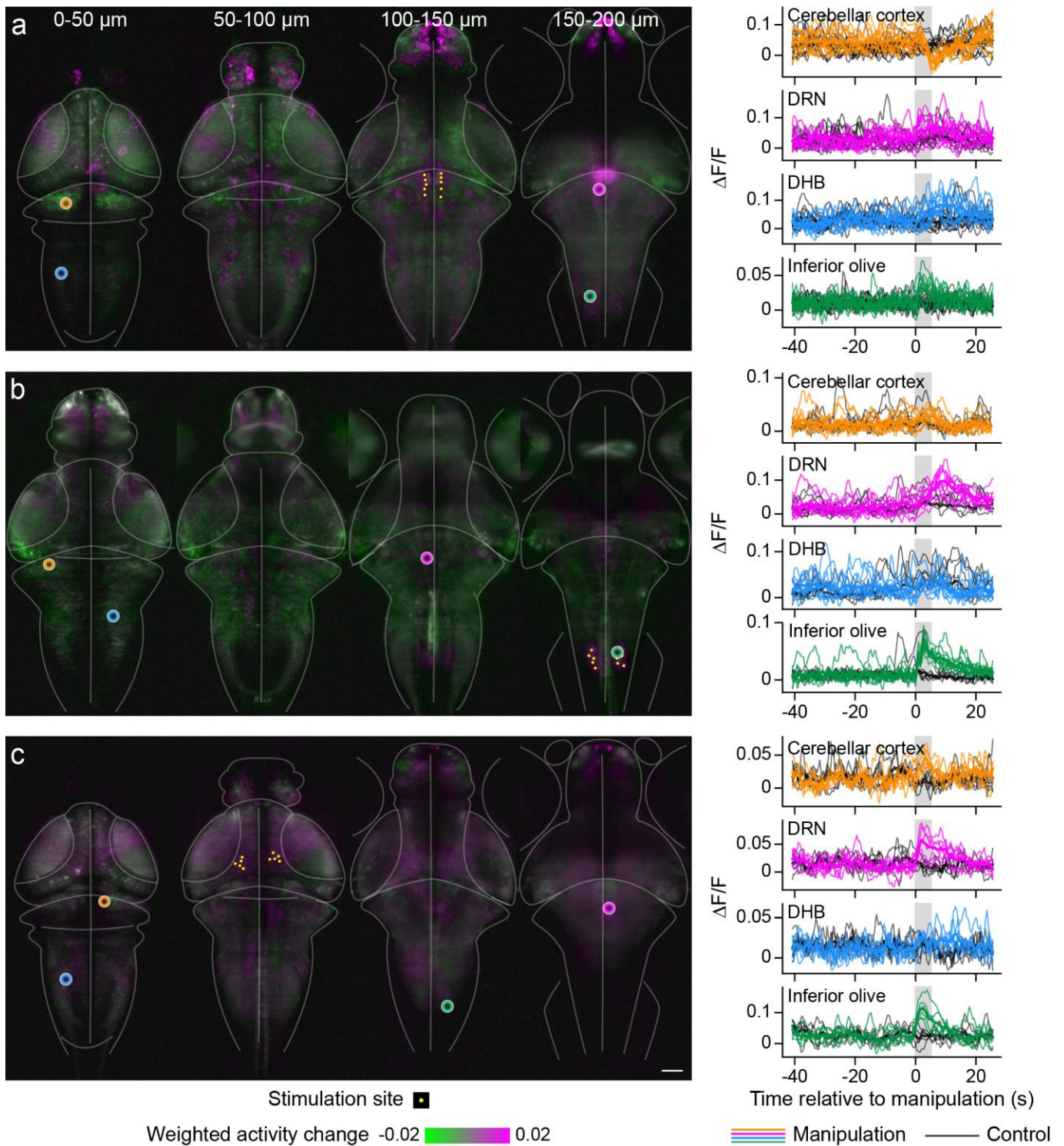
Expression pattern of the HuC::CoChR-eGFP transgenic line

**a**, Slices from a 3D image stack of a 5-day old transgenic zebrafish larva *Tg(elval3:CoChR-eGFP)* expressing the opsin CoChR (Klapoetke *et al.* 2014) in most neurons. The images were acquired with the Opto-SiMView light-sheet microscope.

**b**, Enlarged views of the three regions marked by green boxes in panel a.

The imaging experiment shown in this figure was repeated independently twice with similar results.

Scale bars, 100  $\mu\text{m}$  (a), 10  $\mu\text{m}$  (b).



### Supplementary Figure 8

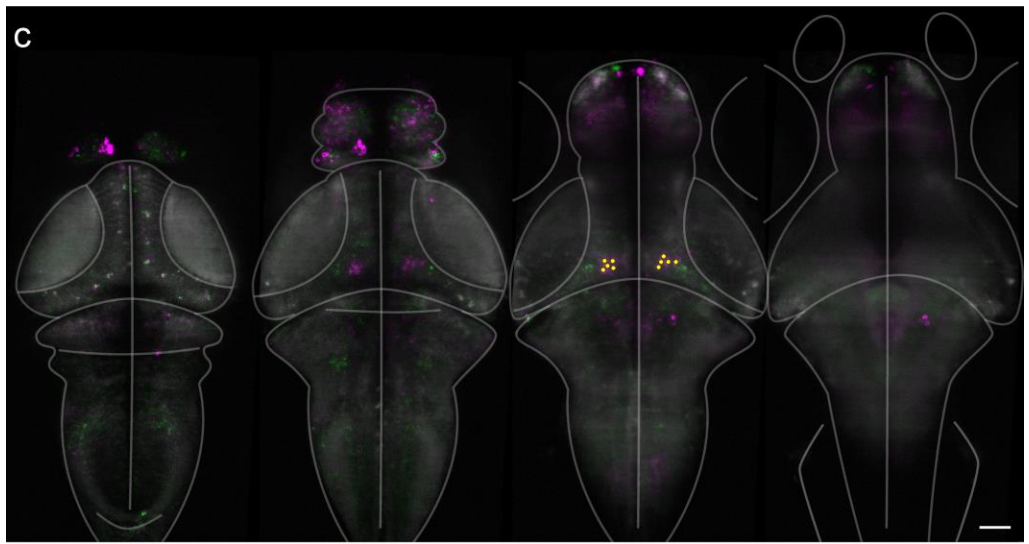
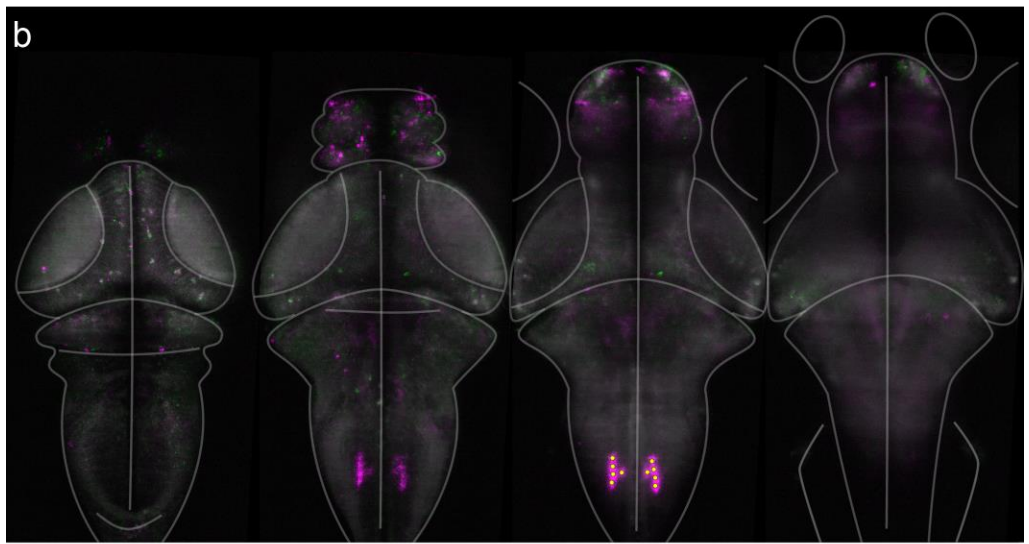
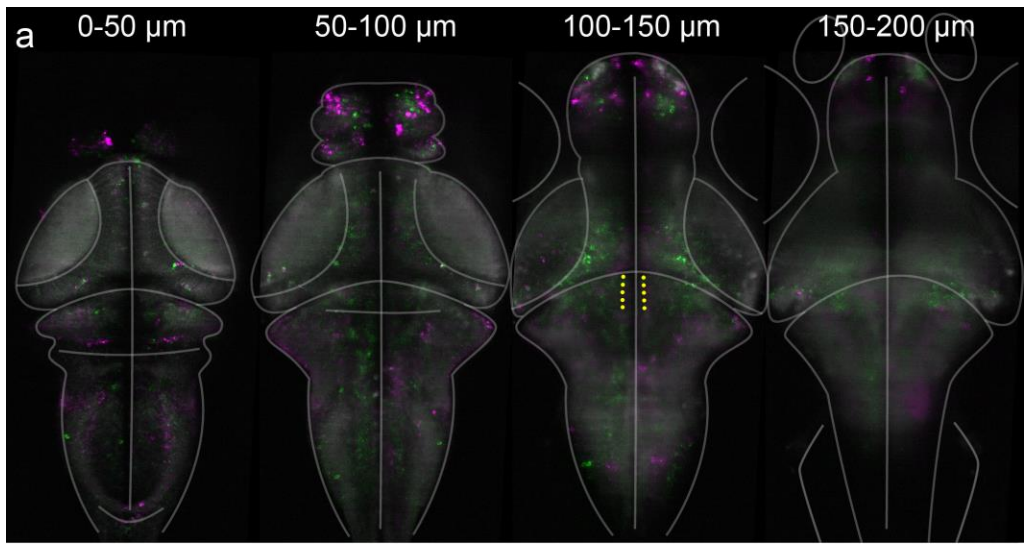
Repetition of optogenetic excitation experiment for an additional specimen

Related to Fig. 6. Optical manipulation of dorsal raphe nucleus (**a**), inferior olive (**b**) and nucleus MLF (**c**) during volumetric functional imaging, using a transgenic line *Tg(elavl3:jRGECO1b) x Tg(elavl3:CoChR-eGFP)*, as in Fig. 6. Targeted cells are indicated by yellow dots and locations of example cell responses by open circles. Shown are four maximum intensity projections, each covering a different 50  $\mu\text{m}$  z-interval of the full image volume (left). The color code indicates the weighted activity change relative to control manipulations, averaged across 12 trials for targets in the DRN, 10 trials for the IO, and 6 trials for the nMLF. Responses are weighted relative to

manipulations targeted to points outside the brain to de-emphasize activity responses that are not well conserved across trials and that are shared between manipulation inside and outside the brain. Control manipulations were targeted to positions outside the brain.  $\Delta F/F$  time traces of the indicated positions (right) show the activity profile of selected single cells (orange, magenta, blue, green) located in the cerebellar cortex, dorsal raphe nucleus (DRN), dorsal hindbrain (DHB) and inferior olive. Traces are shown for all trials (thin colored lines) and controls (thin black lines; for these controls the two-photon laser was targeted just outside the fish's head), as well as for their respective mean (thick lines).

The experiment shown in this figure was repeated independently three times with similar results.

Scale bar, 50  $\mu\text{m}$ .



Stimulation site ■    Weighted activity change -0.02 0.02

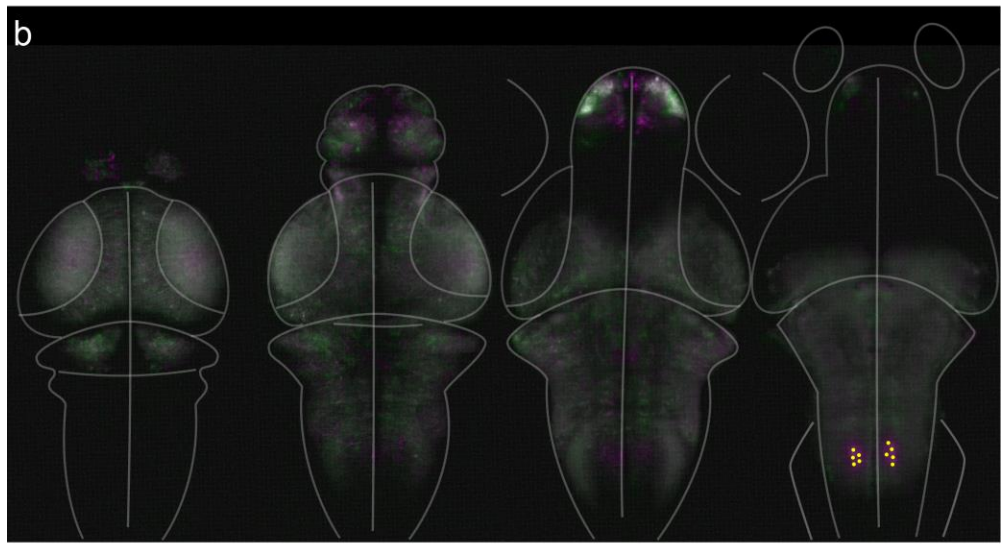
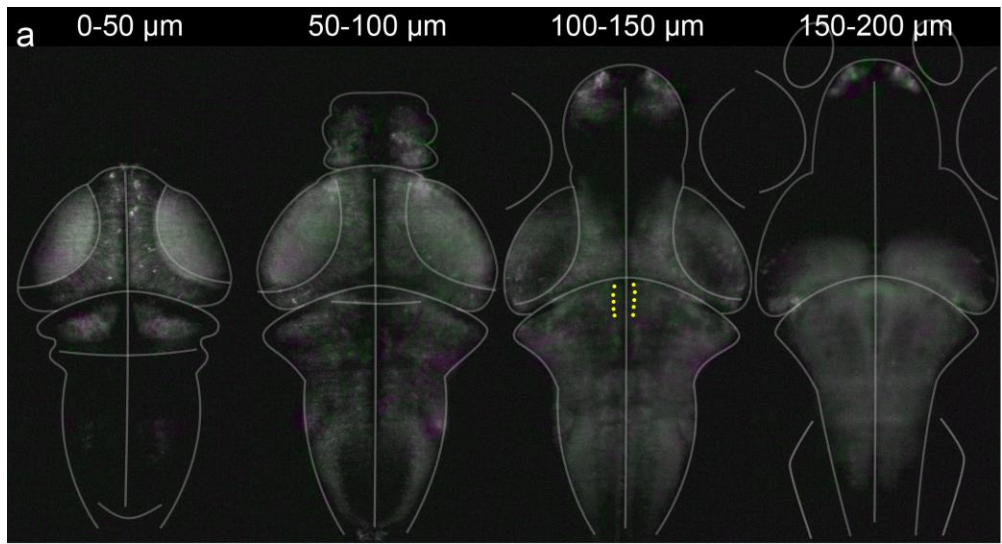
### Supplementary Figure 9

Control optical manipulations during volumetric functional imaging in *Tg( elav13:jRGECO1b)* to test for direct effects of laser exposure, shutter noise, et cetera, on neural activity

Manipulated sites are indicated by yellow dots, targeting the DRN (**a**), IO (**b**) and nMLF (**c**), respectively. The weighted activity change is indicated by a green-magenta diverging color map. Weighting and scaling are identical to **Fig. 6**. Note that the maps are generally dimmer and strong peaks are absent in comparison to **Fig. 6**.

The experiment shown in this figure was repeated independently once with similar results (please see **SI Fig. 10** for the second example).

Scale bar, 50  $\mu\text{m}$ .



Stimulation site ■    Weighted activity change -0.02  0.02

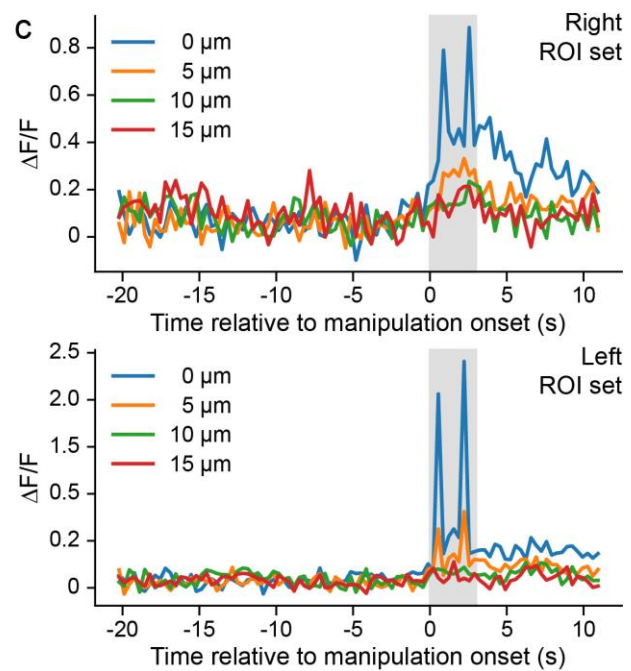
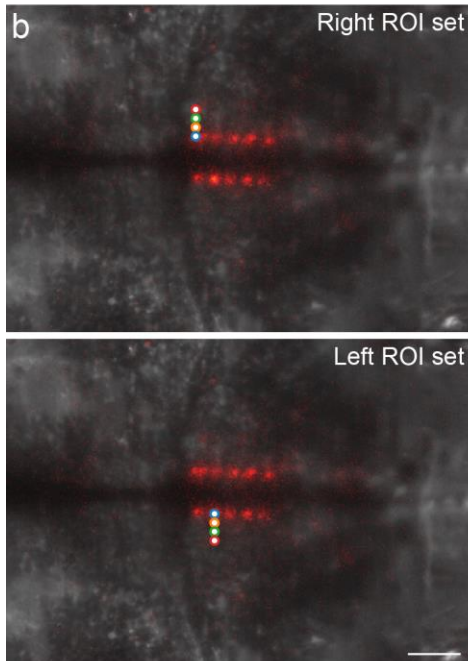
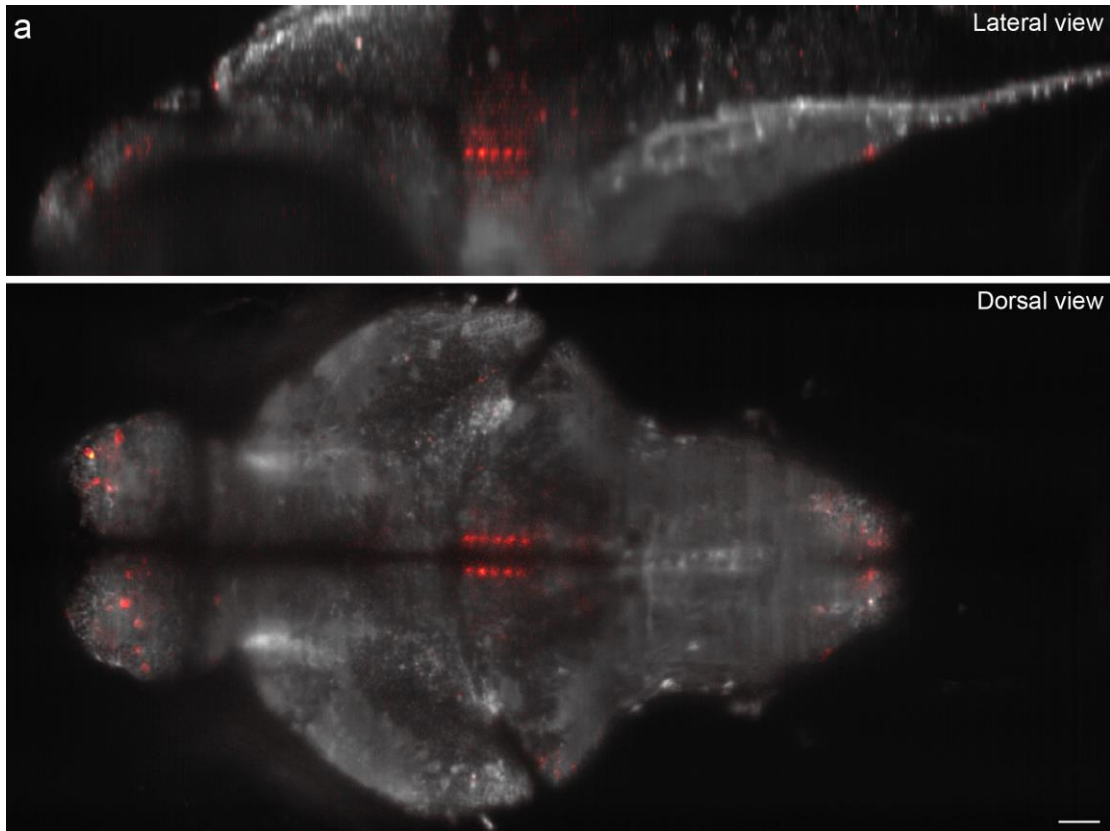
## Supplementary Figure 10

Repetition of control experiment for an additional specimen

Related to Supplementary Fig. 9. Manipulated sites are indicated by yellow dots, targeting the DRN (**a**), IO (**b**) and nMLF (**c**), respectively. The weighted activity change is indicated by a green-magenta diverging color map. Weighting and scaling are identical to **Fig. 6**. Note that the maps are generally dimmer and strong peaks are absent in comparison to **Fig. 6**.

The experiment shown in this figure was repeated independently once with similar results (please see **SI Fig. 9** for the second example).

Scale bar, 50  $\mu\text{m}$ .



### Supplementary Figure 11

#### Spatial confinement of optical manipulation of the DRN

For 9 time points (3 seconds), the sites were targeted iteratively, illuminating each site for 4 ms at a time and jumping between sites within 1 ms.

**a**, Overlay of an anatomical reference (gray, 5th percentile F0 baseline of 159 time points, including 100 time points before manipulation and 50 time points after manipulation) and maximum-projection of  $\Delta F/F$  over these 9 time points (red).

**b**, Selected sites to quantify  $\Delta F/F$  activity traces. Two manipulation sites were selected (blue). For each of these, three sites at increasing distance from the manipulation site were selected as well, in 5  $\mu\text{m}$  increments (orange, green and red, respectively).

**c**, For all sites,  $\Delta F/F$  traces were extracted from pixels in a 2  $\mu\text{m}$  radius (5th percentile constant baseline). Time points with manipulations are indicated with gray background. Since the manipulations occurred concurrently with imaging, the responses are not always recorded directly. For most of the sites, there are only 2 time points where the detection piezo position is exactly pointed at the targeted z-slice while the respective site is activated, resulting in two primary peaks in the respective  $\Delta F/F$  traces.

The experiment shown in this figure was repeated independently three times with similar results.

Scale bar, 25  $\mu\text{m}$ .

## Supplementary Tables

**Supplementary Table 1 | Components of the virtual reality microscope with cell ablation capability (Figs. 1-4)**

Module	Component	Product	Manufacturer
Two-photon ablation module	Infrared femtosecond laser	Coherent Chameleon Ultra II	Coherent
	Pockels cell	Model 350-80LA E-O Modulator	Conoptics
	Set of two orthogonal galvanometric mirrors	Model 6215H Optical Scanner	Cambridge Technology
	F-theta lens	Three f=100 mm achromatic doublets, AC254-100-B, mounted together with 1 mm air gaps, total f = 33 mm	Thorlabs
	Tube lens	CFI second objective lens unit, f=200 mm	Nikon
	Short-pass dichroic mirror	670 nm edge BrightLine multiphoton short-pass dichroic beamsplitter FF670-SDi01-25x36	Semrock
Illumination module (2 modules)	Set of two orthogonal galvanometric mirrors	Model 6215H Optical Scanner. Driver board MicroMax 673XX.	Cambridge Technology
	Illumination laser	SOLE-3 module with Solid-state, PhoXX 488 nm and DPSS lasers 561, 594 nm.	Omicron
	F-theta lens	66-S80-30T-488-1100nm custom lens	Special Optics
	Tube lens	U-TLU-1-2	Olympus
	Piezo objective positioner	P-725.4CD piezo stage E665 piezo amplifier	Physik Instrumente
	Illumination objective	XLFLUOR 4x, NA 0.28	Olympus
	Filter wheel	96A351 filter wheel MAC6000 DC servo controller NDQ neutral density filters	Ludl Melles Griot
Detection module	Detection objective	CFI LWD 16xW, NA 0.8 water-dipping objective	Nikon
	Piezo objective positioner	P-725.4CD piezo stage E665 piezo amplifier	Physik Instrumente
	Detection filter wheel	96A354 filter wheel MAC6000 DC servo controller	Ludl
		525/50 nm BrightLine band-pass filter (diameter 32 mm)	Semrock

	Tube lens	CFI second objective lens unit, f=200 mm	Nikon
	Camera	Orca Flash 4.0 V. 2 (C11440-22C)	Hamamatsu
Specimen positioning system	Motorized stages (2 translation and 1 vertical)	M-521.DD M-511.DD M-501.1PD C-884 Four Axis Motion Controller	Physik Instrumente
Real-time electronics	Computer (PCI) control of PXI boards	PXI-8360 MXI-Express	National Instruments
	I/O interface boards (3 units)	PXI-6733 high-speed analog output board	National Instruments
	BNC connector boxes	BNC-2110 connector block	National Instruments
	Serial interface board	PXI-8432/2	National Instruments
	PXI chassis	NI PIX-1042Q	National Instruments
Control software	LabVIEW 2014 64-bit code	Zebrascope	Coleman Technologies
	LabVIEW functions and device drivers	Vision Development module 2012 NI-RIO NI-Motion NI-VISA NI-Serial	National Instruments
	Visual stimulus presentation and behavior recording	C# program ZebraStimul (available at request)	custom-made
Workstations	Imaging acquisition workstation	SX6750 Workstation Base Platform	Colfax
		2x Intel Xeon E5-2687W 3.1GHz CPUs	Intel
		16x DIMM 16384 MB DDR-3 RAM modules	unspecified
		FireBird Camera Link Deca frame grabber	Active Silicon
		Nvidia Quadro 2000D graphics card	Nvidia
		(2x) Intel 520 Series SSD (SATA) 480GB 6Gbps hard drives (RAID1)	Intel
		(14x) SAS 900GB 6Gbps hard drives (RAID6)	Western Digital
		Intel RS2WG160 SAS RAID controller	Intel

		Intel X520-SR1 PCI-E x 8 10Gb optic fiber network adapter	Intel	
		Windows 7 Ultimate SP1	Microsoft	
	Electrophysiology and stimulus presentation workstation		Intel Core i7-3820 Sandy Bridge-E 3.6GHz CPU	Intel
			ASUS P9X79 PRO motherboard	Asus
			Corsair Vengeance 64GB (8 x 8GB) DDR-3 RAM	Corsair
			NI PCIe-6363 X Series Data Acquisition board	National Instruments
			BNC-2110 shielded connector block	National Instruments
	Sony Pico Mobile Projector (MPCL1)	Sony		
Electro-physiology	Microelectrode Amplifier	Axon Multiclamp 700B	Molecular Devices	
	Manual micromanipulators	MX130	Siskiyou	

## Supplementary Table 2 | Cluster processing time for a typical online analysis using Thunder1.0 Python library

The representative data set used in this performance benchmark contains 11 min of imaging data (1200 z-stacks, 41 planes/stack, 1024x2048 pixels per plane, 16 bit images, a total of 200 GB raw data).

Job type	Cluster processing time (min)		
	10 nodes	20 nodes	30 nodes
Image registration	7	2	2
Conversion into time series and normalization	23	5	2
Linear regression	9	4	4
<b>Total time</b>	<b>39</b>	<b>11</b>	<b>8</b>

**Supplementary Table 3 | Components for the Opto-SiMView microscope for concurrent volumetric imaging and 3D optical manipulation (Figs. 5-6)**

Module/component	Name and product number	Manufacturer
<b>Optical table and breadboard</b>		
Optical table	ST-UT2-48-8 Smart Table (4'x8'x8")	Newport
	High-performance laminar flow isolator S-2000A (4x)	
	Smart Table controller ST-200	
Breadboard	Custom PG2 precision grade breadboard (2'x4'x2.32")	Newport
Rail system	SYS 40 and SYS 65 rail and slide system components	OWIS
<b>Laser</b>		
SOLE-6 engine with dual-fiber head	Solid-state laser (488 nm)	Omicron Laserage
	DPSS lasers (561 nm, 594 nm)	
SOLE-3 engine with dual-fiber head	Solid-state lasers (405 nm, 445 nm)	Omicron Laserage
<b>Illumination system (two modules)</b>		
High-speed laser shutter	LS6ZM2-100 or VS14S2ZM1-100 shutter	Vincent Associates
	VMM-D4 four channel driver	
Illumination filter wheel	96A351 filter wheel	Ludl
	MAC6000 servo controller	
	NDQ neutral density filters OD 1.0, 2.0, 3.0	Melles Griot
	Laser notch filters 488/10, 561/10, 594/10	Chroma
Dual-axis laser scanner	6215HSM40B galvanometer scanner	Cambridge Technology
	MicroMax series 673XX dual axis class 1 integrating servo driver amplifier	
	6 mm XY mirror set, silicon substrate, flatness of $\lambda/4$ , and interconnect cables	
	MK320S-24 power supply	Astrodyne
F-theta scan lens	66-S80-30T scan lens	Special Optics
Illumination tube lens	MXA22018 CFI tube lens	Nikon
Piezo objective positioner	P-628.1CD piezo linear stage, 800 $\mu$ m travel range	Physik Instrumente
	E-665 controller	
Objective base stage and flexure mount system	Aluminum flexure, stainless steel base with integrated spring mechanisms and micrometers	Custom
Illumination water dipping objective	54-12.5-31 objective, 6.4x magnification, NA 0.2	Special Optics
<b>Detection system (two modules)</b>		
Detection filter wheel	96A354 filter wheel	Ludl
	MAC6000 servo controller	
	Band- and long-pass filters	Semrock
Detection tube lens	MXA22018 CFI tube lens	Nikon
Detection objective	CFI75 LWD 16xW/0.8 objective	
Camera	Orca Flash 4.0 v2 camera	Hamamatsu
Piezo objective positioner	P-625.1CD piezo linear stage, 500 $\mu$ m travel range	Physik Instrumente
	E-665 controller	

Objective base stage and flexure mount system	Aluminum flexure, stainless steel base with integrated spring mechanisms and micrometers	Custom
<b>Point-scanning manipulation system</b>		
Titanium-sapphire laser	Chameleon Ultra II, 680-1080nm, 140 fs pulse width	Coherent
Pockels cell	Model 350-80-LA-02 KD*P Series E-O Modulator for use at 700-1200 nm	Conoptics
	Model 102 adjustable modulator mount	
	Model 302RM driver, DC-to-250KHz bandwidth	
Electrically focus tunable lens	EL-10-30-CI-NIR-LD, C-mount thread, NIR coating (700-1100 nm), low dispersion material, integrated temperature sensor 133-872-02	Optotune
	Custom driver for high-speed, high-precision voltage-controlled linear current output and temperature readout	Custom
Dual-axis laser scanner	Model 6220HM44B galvanometer scanner	Cambridge Technology
	MicroMax series 673XX dual axis class 1 integrating servo driver amplifier	
	10 mm XY mirror set, beryllium substrate, flatness of $\lambda/4$ , S4 enhanced durable silver coating	
	MK320S-24 power supply	Astrodyne
F-theta scan lens	66-S80-30T scan lens	Special Optics
Tube lens	49-391-INK lens	Edmund Optics
Relay lens pair	49-361-INK lens	
Dichroic beam splitter	T680 spxr, 5 mm thickness, $\lambda/10$ flatness for transmission, $\lambda/10$ flatness for reflection	Chroma Technology
<b>Specimen positioning system</b>		
Motion controller	C-884.4D motion controller for servo motors	Physik Instrumente
Translation stages	M-111K046 stage with custom mounting pattern	
Rotary stage	Miniature high-resolution 360° rotation stage, closed-loop DC servo motor gearhead	
Sample chamber	Four-objective port chamber with custom-molded rubber seals and overflow protection	Custom

## Supplementary Notes

### Supplementary Note 1 | Additional software packages available upon request

- 1) ZebraScope (LabVIEW), custom microscope control software  
(relies on specific hardware components)
- 2) BehaveAndScan: Visual stimulus presentation and behavior recording (C#)
- 3) AutoDesk assembly file of Zebrascope with ablation arm (.iam and .ipt files)
- 4) Opto-SiMView (LabVIEW), custom microscope control software  
(relies on specific hardware components)

Software developed for activity mapping, brain registration, selection of ablation targets and ablation coordinate correction can be downloaded from GitHub (<https://github.com/optofish-paper>), as described in the main text.